Rayleigh-Bénard convection with rotation at small Prandtl numbers

Kapil M. S. Bajaj and Guenter Ahlers
Department of Physics and Quantum Institute, University of California, Santa Barbara, California 93106

Werner Pesch
Physikalisches Institut der Universität Bayreuth, 95440 Bayreuth, Germany

(Received 7 December 2001; published 16 May 2002)

We present experimental and theoretical results near the onset of the Rayleigh-Bénard convection with rotation about a vertical axis in a fluid with a Prandtl number σ close to 0.18. In the experiment we used a H_2-Xe gas mixture with a separation ratio $\Psi=0.22$ and a Lewis number $\mathcal{L}=1.22$ at various pressures and dimensionless rotation rates Ω up to 400. On the basis of a standard weakly nonlinear stability analysis, we found a supercritical, stationary bifurcation for $\Omega\lesssim 13$, which became subcritical over the range $13\lesssim\Omega\lesssim 160$. For $\Omega\gtrsim 160$ a supercritical Hopf bifurcation precedes the stationary instability of the uniform state. Following the unstable straight-roll fixed point in the subcritical regime by Galerkin methods we determined the location of the saddlenode and the stability of the nonlinear two-dimensional straight-roll state. The rolls were found to be unstable to three-dimensional Küppers-Lortz perturbations for $3.8\lesssim\Omega\lesssim 160$. Theoretical results for a pure fluid with the same σ were qualitatively similar. Measurements using shadowgraph flow visualization yielded a bifurcation line and an Ω range of subcriticality, which agreed with the stability analysis. In the subcritical range the experiment revealed a discontinuity of the pattern amplitude at onset, but was unable to find any hysteresis. Patterns at onset fluctuated irregularly between the ground state and the finite-amplitude state. In this parameter range the convection pattern further above onset was chaotically time dependent. Investigation of the Hopf bifurcation line was difficult because of a wall mode that, for large Ω, preceded the bulk instability. For $\Omega\simeq 400$, patterns were found in the sample interior only when the expected Hopf bifurcation was exceeded by about 10%. This is consistent with the convective nature of the bifurcation. However, the observed structure, although time periodic, was spatially disordered and had a frequency that was considerably larger than the expected Hopf frequency. In a separate sample cell with a radial ramp in the spacing no structure was observed at all in the cell interior until the expected stationary instability was reached.

DOI: 10.1103/PhysRevE.65.056309 PACS number(s): 47.54.+r, 47.20.Lz, 47.27.Te

I. INTRODUCTION

Convection in a thin horizontal layer of fluid heated from below, known as Rayleigh-Bénard convection (RBC), is perhaps the most thoroughly studied pattern-forming system [1,2]. The spatially uniform conduction state becomes unstable to convection when the Rayleigh number

$$R=\alpha g d^3\Delta T/\kappa\nu \tag{1}$$

reaches a critical value R_c [3]. Here α is the isobaric thermal expansion coefficient, g is the acceleration of gravity, d is the fluid layer thickness, κ is the thermal diffusivity, ν is the kinematic viscosity, and ΔT is the temperature difference across the fluid. RBC offers unique opportunities to examine a number of bifurcation and pattern-formation phenomena. We focus on the effect of rotation with an angular frequency $2\pi f$ about a vertical axis [4] where f is the rotation frequency in hertz. In that case, interesting differences between theory and experiment exist, which remain unresolved at this time, and a number of theoretically predicted phenomena have not yet been observed in the laboratory.

One of the interesting aspects of this system is that, over a wide parameter range, spatiotemporal chaos (STC) is entered immediately above onset via a supercritical bifurcation. In this weakly nonlinear state of STC, first predicted by Küppers and Lortz (KL) for dimensionless rotation rates $\Omega\equiv 2\pi f d^2/\nu$ above a critical value $\Omega_{KL}=O(10)$, rolls are unstable to another set of rolls with an angular orientation relative to the first, which is advanced in the direction of rotation by an angle θ_{KL} [5]. This instability has been the subject of several recent experimental investigations for small $\Omega\lesssim 20$, using compressed gases with Prandtl numbers $\sigma\equiv\nu/\kappa$ near one as the working fluid [2]. The predicted [5,6] supercritical nature of the stationary bifurcation to the KL state has been confirmed quantitatively by the detailed experiments of Hu *et al.* [7,8]. However, these studies disagree with relevant weakly nonlinear theories in the form of Ginzburg-Landau (GL) equations. The time and length scales of the KL state in the experiments do not have the expected power law dependence on the reduced control parameter $\epsilon=\Delta T/\Delta T_c-1$. Moreover, the chaotic KL dynamics is expected to persist near the onset for all $\Omega>\Omega_{KL}$. Again, contrary to theoretical expectations, patterns with fourfold coordination were found near onset in recent experiments [9] and in direct numerical integrations of the Boussinesq equations [2] when $\Omega\gtrsim 70$. Over some parameter ranges the system formed a near-perfect square lattice that rotated slowly relative to the experimental cell. These discrepancies between experiments and theory remain unresolved.

The range $\sigma\lesssim 0.7$ remains largely unexplored by experiment because representative fluids are difficult to find. Pure gases generally have $\sigma\gtrsim 2/3$ (the hard-sphere gas value), and classical liquids have $\sigma>1$. Although σ vanishes at the su-

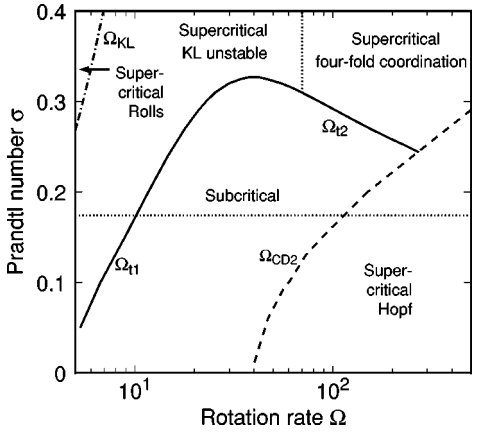

FIG. 1. The bifurcation diagram for an infinitely extended pure fluid as a function of σ and Ω. All lines in the diagram were obtained theoretically, except for the near-vertical dotted one that gives the approximate experimentally determined location of the transition from the KL state to the fourfold-coordinated state at onset and the horizontal dotted one that indicates the parameter range explored in the present study. The dash-dotted line labeled Ω_{KL} shows the transition from straight rolls to Küppers-Lortz or domain chaos at onset. The solid line labeled Ω_{t1} and Ω_{t2} is the tricritical line that separates the supercritical from the subcritical bifurcation range. The dashed line labeled Ω_{CD2} is the line of codimension-two points where the Hopf bifurcation meets the stationary bifurcation.

perfluid transition of liquid ^{4}He, experiments with this fluid, especially with rotation about a vertical axis, are complex and flow visualization is difficult. Values of σ of order 10^{-2} are accessible with liquid metals; but the range $10^{-2}<\sigma \lesssim 0.7$ is not represented by pure classical fluids. However, recently it was recognized that values of σ as low as 0.17 can be reached in gas *mixtures* [10], thus opening up a parameter range with interesting new phenomena. For $\sigma<0.33$ the predicted bifurcation diagram for RBC with rotation is very rich [3,6,11–14]. For *pure* fluids it is shown in Fig. 1 [15]. In Sec. III we show that qualitatively it does not change for our gas mixture. At small $\Omega<\Omega_{t1}$, the stationary bifurcation is expected to be supercritical. In this range the KL state is predicted above $\Omega_{KL}\simeq 5<\Omega_{t1}$. Over the intermediate range $\Omega_{t1}\lesssim\Omega\lesssim\Omega_{t2}$ the bifurcation is predicted to be *subcritical* [11,6,12]. Here the finite-amplitude nonlinear state above the bifurcation is also expected to be KL unstable. As is seen in Fig. 1, the subcritical range depends on σ.

For sufficiently large Ω the stationary bifurcation is predicted to be preceded by a supercritical Hopf bifurcation [3]. The locus $\Omega_{CD2}(\sigma)$ where the stationary and Hopf bifurcations meet is a codimension-two (CD2) line in the σ-Ω plane. So far the Hopf bifurcation has not been accessible in experiments because $\Omega_{CD2}(\sigma)$ diverges with increasing σ at $\sigma=0.677$ [3,12] and because smaller σ values are difficult to achieve, particularly in large-aspect-ratio cells and with flow visualization.

In this paper we focus on rotating convection for σ near 0.18. This value is close to the lowest accessible value with compressed gases, and was obtained by using a mixture of H_2 and Xe with a mole fraction X close to 0.5 [10]. Visualization of the flow patterns was achieved with the shadowgraph method. A weakly nonlinear stability analysis of the Boussinesq equations for the mixture was carried out for comparison with the experiment. For this σ, we found theoretically that the stationary-bifurcation branch near Ω_{t2} is preceded by the Hopf bifurcation, with the CD2 bifurcation at $\Omega_{CD2}\simeq 200$. In the experiment Ω values up to 400 could be obtained; thus the entire subcritical range and a significant part of the predicted Hopf range were accessible.

In agreement with our calculations, we found that the bifurcation is supercritical for $\Omega<\Omega_{t1}\simeq 13$ and subcritical for larger Ω. Near but below Ω_{t1} the nonlinear state at onset was chaotic, as expected above $\Omega_{KL}\simeq 3.8$. For $\Omega_{t1}<\Omega\lesssim 50$ we found a chaotically time-dependent state that appeared discontinuously with a finite amplitude at onset, but surprisingly we found no hysteresis. Directly *at* onset, the system fluctuated intermittently between the chaotic convecting state and the ground state. For $\Omega\gtrsim 50$ the amplitude increased dramatically just above onset, but it was not possible to identify a clear jump in the experiment. Although we searched for it at Ω up to about 400, we were unable to find a clear signature of the time-periodic pattern, which should have resulted from a Hopf bifurcation.

II. EXPERIMENTAL METHOD AND APPARATUS

Our apparatus is described in detail elsewhere [16]. We used cylinderical cells of aspect ratios $\Gamma\equiv$radius/height $=8.3$ and 11 with the same height $d=4.00\pm 0.02$ mm. The bottom of each cell was a diamond-machined [17] aluminum plate. The top plate was an optically flat sapphire. A porous cardboard ring was sandwiched between the plates for the sidewall. The sample was a commercially available high-purity mixture of H_2-Xe. The quoted molar ratio of H_2-Xe was 0.496:0.504. The apparatus was mounted on a rotating table. A shadowgraph tower was mounted axisymmetrically on top of the apparatus to enable imaging in the rotating frame. The direction of rotation of the whole assembly was counterclockwise when viewed from above. The physical angular rotation frequency $\omega_d=2\pi f$ was scaled by the vertical viscous diffusion time $\tau_\nu=d^2/\nu$ to yield the dimensionless rotation frequency $\Omega\equiv\omega_d\tau_\nu$. Increasing the pressure decreases ν and hence increases τ_ν. Typically, τ_ν was between 25 s and 70 s, depending on the pressure and the mean temperature. We used pressures of 10–45 bars that were held constant to within about a millibar. With a reasonable choice of pressure and cell height it was possible to explore the Ω range from zero up into the Hopf regime.

Most of the experiments were carried out at pressures of 16.2 bars. With $\tau_\nu=27.5$ and ω_d up to 5.82 rad/s, this pressure allowed us to explore $\Omega\lesssim 160$. For higher Ω up to 400, we used a pressure of 40 bars. Varying the pressure had only a small effect on σ, which varied in the range of 0.174 (at small pressures) to 0.185. The samples all conformed well to the Boussinesq approximation; the Boussinesq parameter Q [18] varied from 0.066 to 0.49 over the whole range. The maximum Froude number, $F\equiv r\omega_d^2/g$, which measures the effect of the centrifugal acceleration, was less than 0.15. Here $r=\Gamma d$ is the radius of the cell. For our mixture the

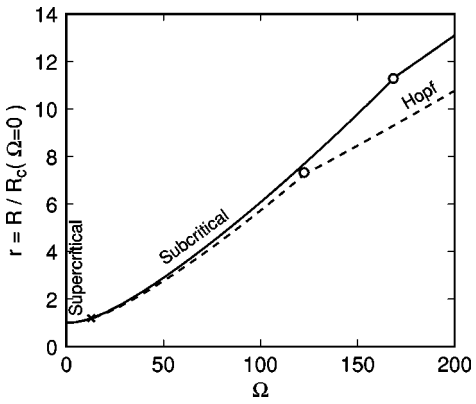

FIG. 2. The theoretical critical Rayleigh numbers $r_c = R_c(\Omega)/R_c(0)$ as a function of Ω for $\sigma = 0.174$ for a pure fluid (dashed line) and for a mixture with $\Psi = 0.22$ and $\mathcal{L} = 1.22$ (solid line). The small $\times$ shows the lower tricritical point at Ω_{t1} of the mixture, which is nearly indistinguishable from the pure case. The circles give the CD2 points. The upper tricritical points are located above Ω_{CD2}, and are thus preempted by the Hopf bifurcation. The stationary bifurcation lines are independent of σ.

relevant binary-mixture parameters (see Sec. III) were $\Psi = 0.22$ and $\mathcal{L} = 1.22$. These were the same within 1% for all the runs.

The temperature of the bath was fixed at 37.5 °C. At each Ω, the temperature of the bottom plate was raised quasistatically above $\Delta T_c(\Omega)$ in small steps. The temperatures were regulated to achieve a stability of ΔT of better than 10^{-3} °C. At each step we waited for 2 h, which is much longer than $\Gamma^2 \tau_v (\simeq 1/2$ h), for the system to reach a steady state. The smallest ΔT step used was 5 mK. After reaching the highest ΔT, ΔT was lowered in small steps below onset to obtain data for both increasing and decreasing ϵ. The typical ϵ range explored was $-0.05 \lesssim \epsilon \lesssim 0.1$, although some runs went to larger ϵ.

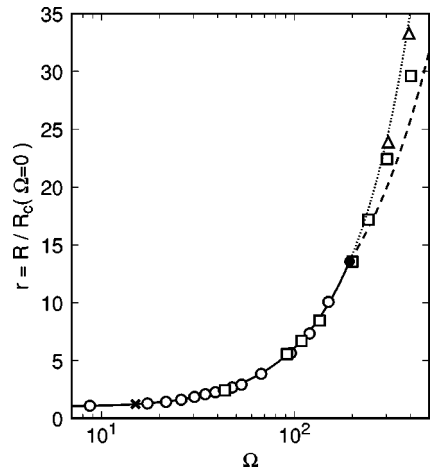

FIG. 3. The reduced critical Rayleigh number $r_c = R_c(\Omega)/R_c(0)$ for $\Psi = 0.22$ and $\mathcal{L} = 1.22$ as a function of Ω on a logarithmic scale. Circles (squares and triangles) are experimental values for $\sigma = 0.174$ (0.185). The stationary bifurcation (solid and dotted lines) is independent of σ. The lower tricritical point ($\times$), the codimension-two point (solid circle), and the Hopf bifurcation (dashed line) are shown for $\sigma = 0.185$.

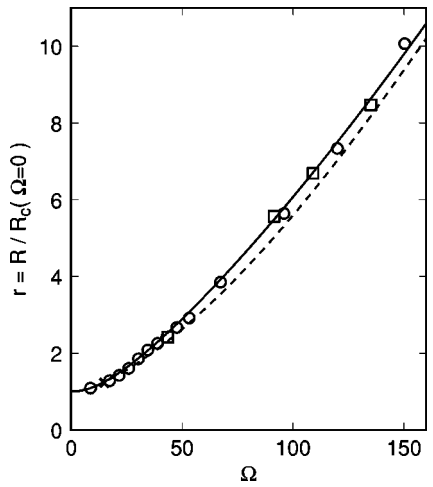

FIG. 4. A more detailed plot on a linear Ω scale of the reduced critical Rayleigh number r_c at intermediate Ω. The symbols and solid line have the same meaning as in the previous figure. The dashed line is the calculated location of the saddlenode for the unstable straight rolls and $\sigma = 0.174$.

Usually, a large number of images (up to 2048/step) of a central square part of the cell were analyzed in real time for each ΔT. The inscribed square had a diagonal that was 91% of the cell diameter. The images were taken at a constant time interval of about $\tau_\kappa = \sigma \tau_v$ (≈ 5 s). At large $\Omega \gtrsim 100$, where a bifurcation to a wall mode [19] preceded the bulk bifurcation and where this mode occupied a significant fraction of the cell, a smaller square unencumbered by this mode was analyzed. While searching for the Hopf regime we also took images of the entire circular cell.

III. THEORY

Our theoretical analysis of convection patterns is based on the standard hydrodynamic description, i.e., the generalized Boussinesq equations with rotation for binary mixtures. As usual, the system is idealized to be laterally infinite. A linear analysis yields the critical properties (critical wave number, Rayleigh number, Hopf frequency) of the rolls bifurcating at onset. The finite-amplitude states above onset and their stability are determined by using a weakly nonlinear analysis and a fully nonlinear Galerkin approach. The main results are contained in Figs. 1–4 and Table I. Further details are found in the Appendix.

The calculations concentrated on a pure fluid with $\sigma = 0.174$ and on binary mixtures with $\sigma = 0.174$ and 0.185. These values correspond to most of the experimental runs. For mixtures (see also the Appendix), additional parameters are required to describe the nature of the convecting state because of the coupling between the concentration and temperature fields [20]. The temperature gradient changes the concentration field because of diffusion. This so-called Soret effect is characterized by the separation ratio

$$\Psi \equiv -\frac{\beta}{\alpha}\frac{k_T}{T} = -\frac{\beta}{\alpha} C(1-C) S_T, \tag{2}$$

TABLE I. Parameter values of special bifurcation points for a pure fluid, and for the binary mixture with $\Psi=0.22$ and $\mathcal{L}=1.22$. The subscripts KL, $t1$, and $CD2$ are explained in the caption of Fig. 1.

	σ	Pure fluid	Mixture
$R_c(\Omega=0)$		1707.8	1131.0
Ω_{KL}	0.174	3.67	5.08
r_{KL}	0.174	1.015	1.032
r_{t1}	0.174	1.113	1.192
Ω_{t1}	0.174	10.15	12.83
r_{t1}	0.185	1.127	1.224
Ω_{t1}	0.185	10.79	13.93
r_{CD2}	0.174	7.32	11.28
Ω_{CD2}	0.174	122.4	168.4
r_{CD2}	0.185	8.32	13.68
Ω_{CD2}	0.185	138.0	197.2

where β is the solutal expansion coefficient, k_T the thermal diffusion ratio, T the temperature, C the mass concentration of the heavier component, and $S_T=k_T/[C(1-C)T]$ the Soret coefficient. The quantity k_T is defined so that the heavier component moves to the cold (hot) region when $k_T>0$ ($k_T<0$). When $\Psi>0$, the induced concentration gradient is destabilizing the conduction state and the critical Rayleigh number is reduced, i.e., $R_c(\Psi)<R_c(0)$.

An additional parameter arises in binary mixtures because the dynamics of the concentration variable is associated with an independent time scale governed by the concentration diffusivity D. Thus the Lewis number

$$\mathcal{L}\equiv D/\kappa \tag{3}$$

is important and serves as a measure of the ratio of the mass-diffusion time to the thermal-diffusion time. In binary-gas mixtures, $\mathcal{L}=O(1)$. For $\Omega=0$ the pattern immediately above R_c then consists of rolls like those in pure fluids [10]. In the calculations we used $\Psi=0.22$ and $\mathcal{L}=1.22$, which corresponds to the mixtures used in the experiment [10].

An important question is whether RBC in mixtures with rotation behaves similarly to the pure-fluid case with the same σ. For $\mathcal{L}=O(1)$ and positive Ψ we found that R_c was reduced as expected, but that the bifurcation lines when expressed in terms of $r_c=R_c(\Omega)/R_c(0)$ as well as the nature of the instabilities do not differ qualitatively from those of a rotating pure fluid. This is consistent with general considerations because for $\mathcal{L}=1$ the time scales of heat diffusion and mass diffusion are equal, and because for positive Ψ both diffusion processes lead to destabilization of the conduction state.

The results for the pure fluid and for the mixture with $\sigma=0.174$ are presented in Fig. 2. It is clear that both have similar Ω ranges for the supercritical, subcritical, and Hopf bifurcations. However, there are quantitative differences. The largest difference is found in the location of the CD2 point and the Hopf-bifurcation line. Precise values for the special bifurcation points are given in Table I. We note that the stationary bifurcation lines depend on Ψ and $\mathcal{L}$, but not on σ. The Hopf bifurcation line, on the other hand, depends on σ as well. Thus the shift of the CD2 point with σ is a consequence of a shift of the Hopf bifurcation line. All the nonlinear properties, i.e., the location of the tricritical bifurcation and of the saddlenode in the subcritical region, depend on σ as would be expected.

IV. RESULTS

At small Ω where the bifurcation is supercritical, we determined $\Delta T_c(\Omega)$ at the onset of convection from the contrast of the shadowgraph images as described, for instance, in Ref. [7]. At larger Ω where the bifurcation is subcritical and the pattern is chaotic, a different method was required. There we determined a time average $\langle A_m\rangle(\Delta T)$ of the maximum local amplitude $A_m(t,\Delta T)$ of the pattern, and located the jump or rapid rise of $\langle A_m\rangle(\Delta T_c)$ [21].

There was no hysteresis, and thus the change of $\langle A_m\rangle$ yielded an experimentally well defined onset that could be resolved with a precision of 10^{-3} to 10^{-2} in ϵ, depending on the Ω range; but it is unclear whether this onset should be identified with the limit of stability of the basic state or with some other point below this limit but above the saddlenode of a subcritical bifurcation. Nonetheless, since this dicontinuity is the only experimentally well defined signature of the onset of convection, we refer to it as ΔT_c and used it to compute all ϵ values.

Since our samples all conform well to the Boussinesq approximation (see Sec. II), we have to a very good approximation $\Delta T_c(\Omega)/\Delta T_c(0)=R_c(\Omega)/R_c(0)\equiv r_c$. Results for r_c derived thus from $\Delta T_c(\Omega)$ are shown in Fig. 3 over the entire experimental range of Ω on a logarithmic horizontal scale. The solid line is the theoretical result for r_c in the stationary regime. Above Ω_{CD2} the Hopf bifurcation line (dashed line) precedes the stationary one (dottedline). The data for intermediate Ω values are shown in more detail in Fig. 4. Shown as well, as a dashed line in Fig. 4, is the calculated location of the saddlenode r_{sa} for the unstable straight rolls that form at the subcritical bifurcation. For $\Omega\lesssim 200$ the data agree well with the calculation of r_c for the laterally infinite system. For larger Ω, where a primary Hopf bifurcation is expected, the agreement with the calculation is not as good. We will return to this problem later in this paper.

For $\Omega\lesssim 12$, we observed the expected supercritical bifurcation to the KL state. There was no hysteresis, and the shadowgraph contrast grew continuously as ϵ was increased beyond zero. A time series of images for $\Omega=8.7$ and $\epsilon=0.035$ at time intervals of $26.2\tau_\nu$ is shown in Fig. 5. Unlike experiments with larger Γ [2], we had only one domain of rolls in the cell. The rolls changed orientation with time as is expected for the KL state. We did not study this parameter range any further. A more detailed investigation using a cell with a larger Γ would be of interest.

The range $17\lesssim\Omega\lesssim 50$ covers interesting new pattern-formation phenomena above the subcritical bifurcation. A time series of patterns for $\Omega=44$ just above the onset at $\epsilon\simeq 0.004$ is shown in Fig. 6. The pattern dynamics was intermittent, switching irregularly between a spatially disordered large-amplitude state and a state of much smaller amplitude

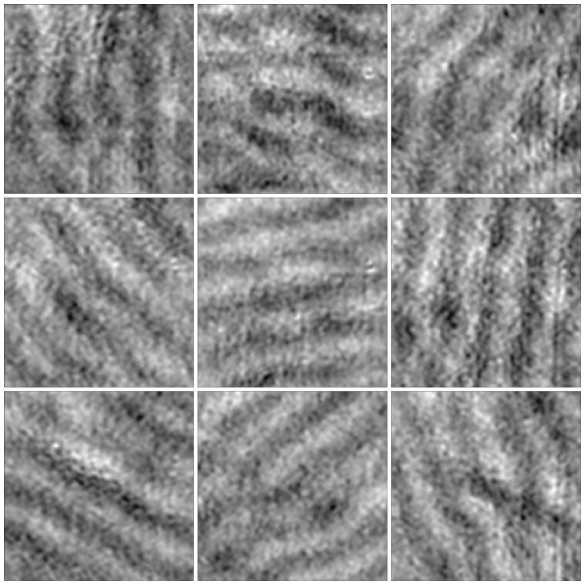

FIG. 5. A time series (from left top to right) of shadowgraph images for $\Omega=8.7$ and $\epsilon=0.035$ at intervals of 720 s or $26.2\tau_\nu$. The size of each image is $5.9d\times5.9d$.

consisting of circular time independent rolls. The origin of the small-amplitude circular pattern is unclear. It could be caused by thermal sidewall forcing [7], or it could be due to coupling between the Rayleigh-Bénard instability and a weak large-scale radial flow induced by the centrifugal force. It was observed well below onset, and we will refer to it as the ''ground state.'' The pattern stayed in the ground state (large-amplitude state) for long irregular time intervals, and jumped to the large-amplitude state (ground state) randomly. The high-amplitude pattern, once established, had a chaotic dynamics with a typical time scale close to the vertical thermal diffusion time τ_κ. As is evident from Fig. 6, the patterns

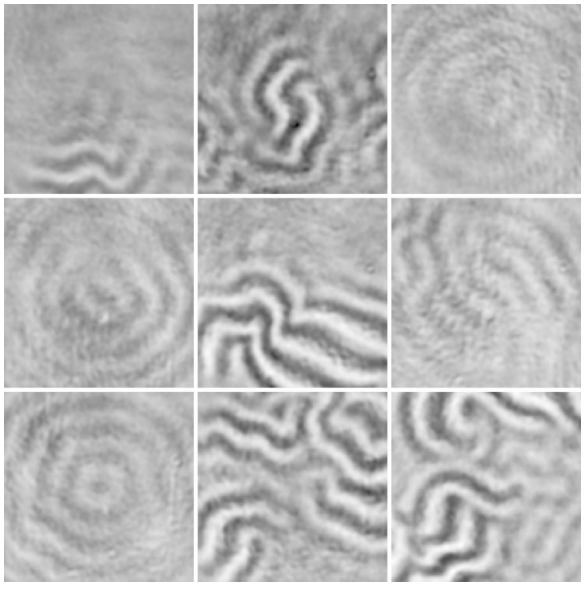

FIG. 6. Time series (from top left to right) of images for $\Omega=44$ and $\epsilon\simeq0.004$ at time intervals of 960 s or $200\tau_\kappa$. The size of each image is $5.9d\times5.9d$.

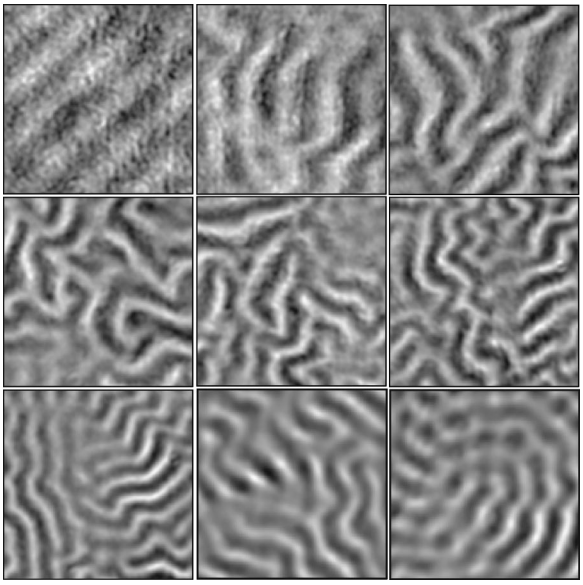

FIG. 7. Images for fairly small ϵ at various Ω. From left to right and then top to bottom, the (Ω,ϵ) values are (9,0.052), (22,0.016), (30,0.039), (39,0.041), (48,0.038), (52,0.052), (67,0.041), (96,0.055), and (120,0.02). The size of all but the last two images is $5.9d\times5.9d$. For $\Omega=96$ and 120 the size of the images is $4.1d\times4.1d$.

could be localized with some of the cell in the ground state, or they could be extended, nearly or completely filling the cell.

At very slightly larger ϵ the pattern always remained in the high-amplitude state, i.e., it ceased being intermittent, and it always filled the entire cell; but its appearance and time dependence remained similar to the images shown in Fig. 6. Above onset, say for $\epsilon\gtrsim0.04$, the qualitative nature of the pattern depended very little on Ω. A sequence of images at various Ω and small ϵ is shown in Fig. 7. One sees that the characteristic wavelength of the rolls decreases with increasing Ω.

In order to illustrate the pattern evolution with ϵ, we present in Fig. 8 examples at several ϵ for $\Omega=30.3$. Again the qualitative nature of the patterns does not change much,

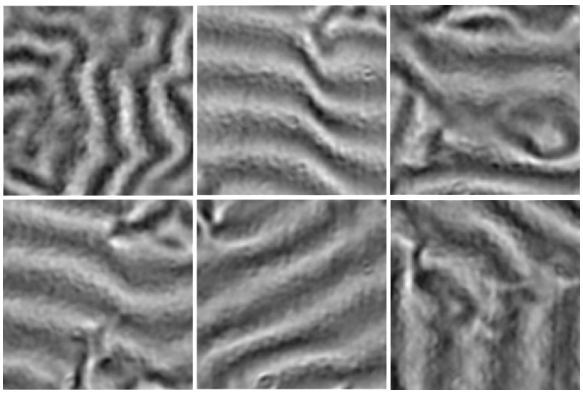

FIG. 8. Images for $\Omega=30.3$ at various ϵ. From left to right and then top to bottom, the ϵ values are 0.034, 0.182, 0.33, 0.43, 0.48, and 0.63. The size of each image is $5.9d\times5.9d$.

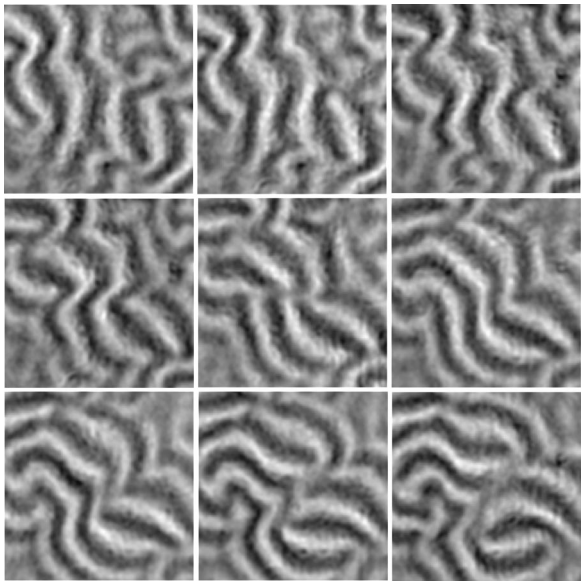

FIG. 9. A time sequence of images for $\Omega=30.3$ and $\epsilon=0.034$. From left to right and then top to bottom, they are at intervals of 4.2 s ($0.75\tau_\kappa$). The size of each image is $5.9d\times5.9d$.

although the characteristic wavelength of the rolls increases with ϵ.

In Figs. 9 and 10 we illustrate further the dynamics of the patterns by showing time sequences at $\epsilon=0.034$ and 0.63, respectively, both for $\Omega=30.3$. In both cases, as well as over a wide Ω range, a typical aspect of the dynamics is a wavy disturbance of the rolls which, with growing amplitude, culminates in local pinching and disconnection of rolls. This is particularly evident, for instance, in the middle of the third and fourth images of Fig. 9. This process usually is followed by reconnection to the previously adjacent rolls as seen in the fifth and sixth images of Fig. 9. Such an event typically

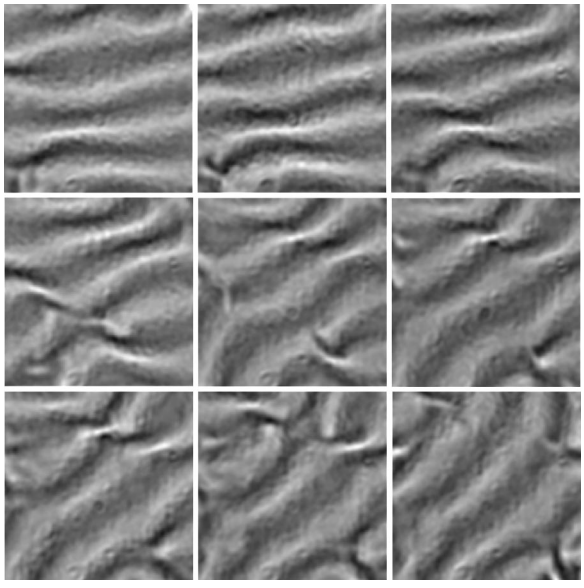

FIG. 10. A time sequence of images for $\Omega=30.3$ and $\epsilon=0.63$. From left to right and then top to bottom, they are at intervals of 4.2 s ($0.75\tau_\kappa$). The size of each image is $5.9d\times5.9d$.

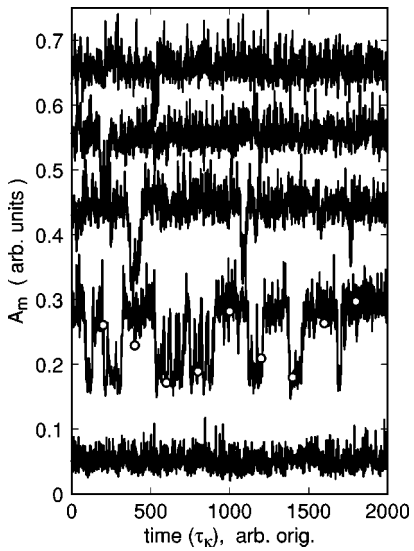

FIG. 11. Time series of the maximum shadowgraph amplitude A_m for $\Omega=44$. From bottom to top, the data are for $\epsilon=-0.004$, 0.004, 0.008, 0.015, 0.019. Starting at $\epsilon=-0.004$, the data are upshifted by 0.0, 0.1, 0.2, 0.3, 0.4 for the successive ϵ values. The circles are A_m for $\epsilon=0.004$ and correspond to the times of the images in Fig. 6.

results in a net rotation of the pattern. This dynamics has significant similarity to that found in the numerical work of Ref. [13] and displayed in Figs. 10 and 11 of that reference.

To characterize the transition to the large-amplitude state, we show in Fig. 11 several time series of the maximum local pattern amplitude $A_m(t)$ for $\Omega=44$. The lowest curve is for $\epsilon=-0.004\pm0.002$. It is just below onset and samples only the low-amplitude circular ground-state pattern. The next one was shifted upward by 0.1 for clarity. It is just above onset, for $\epsilon=+0.004\pm0.002$. It shows the fluctuations between the ground state and the large-amplitude state illustrated by the images in Fig. 6. The actual values of A_m coresponding to these images are shown as open circles. The third data set was displaced vertically by 0.2 and corresponds to $\epsilon=0.008$. Although there are still a few fluctuations, they have become quite rare and the system finds itself mostly in the convecting state. Two more traces are shown, each upshifted by another 0.1 relative to the previous one to avoid overlap. They are for $\epsilon=0.015$ and 0.019 and show that the fluctuations died out once the system was a percent or so above onset.

For $\omega=44$, the time average $\langle A_m\rangle(\Delta T)$ of $A_m(\Delta T,t)$ is shown as a function of ϵ in Fig. 12. The open (solid) circles are for increasing (decreasing) ΔT. One sees that, within our resolution of about 0.002 in ϵ, there is no hysteresis at the transition even though there is a large, sharp jump in $\langle A_m\rangle$. The background level for $\epsilon<0$ is due in part to the experimental noise, and in part to the weak concentric pattern below onset.

In Fig. 13 we show the results for $\langle A_m\rangle$ for a few selected Ω values. Over this entire range of Ω, $\langle A_m\rangle$ shows a jump ΔA_m at onset, which increases monotonically with increasing Ω. We conclude that the bifurcation is subcritical even though there is no hysteresis. For $\epsilon<0$, the background tends

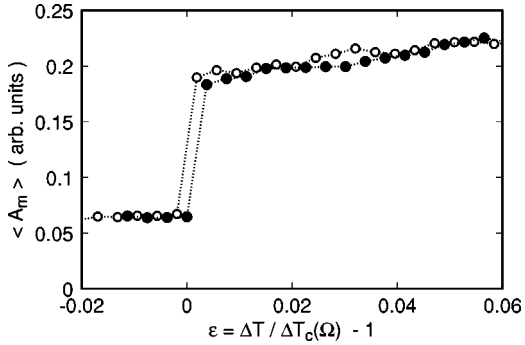

FIG. 12. The time average $\langle A_m \rangle(\Delta T)$ of $A_m(\Delta T,t)$ for $\Omega = 44$. Open (solid) circles were obtained with increasing (decreasing) ΔT. These data illustrate the absence of hysteresis.

to grow with Ω. This suggests that the contribution from the small-amplitude circular pattern (which accounts for part of this background) may be due to the centrifugal force.

On the basis of a Landau model for tricritical points we expect $(\Delta A_m)^2 = g_0 \times (\Omega - \Omega_{t1})/k$ for the jump of the amplitude at $\epsilon = 0$. Here $g_0 \times (\Omega - \Omega_{t1})$ is the cubic and k the quintic coupling coefficient. Thus, within this simple model, $(\Delta A_m)^2$ should be linear in Ω. A plot of the experimental data as a function of Ω is shown in Fig. 14(a). They can be described by a straight line only if the point at $\Omega = 17.3$ is ignored. Then a fit to the remaining data (dashed line in the figure) gives $\Omega_{t1} = 22.0$, which does not agree too well with the theoretical result $\Omega_{t1} = 12.8$ shown by the open circle. A problem with this interpretation is that the data for $\Omega = 17.3$ suggest that the bifurcation is still subcritical at that rotation rate. This can be seen more clearly in Fig 15 that gives the results very near the onset for the two lowest Ω values. A better fit to all the data is illustrated in Fig. 14(b) where (ΔA_m) (rather than its square) is shown as a function of Ω. The data suggest a linear dependence, and a straight-line fit [solid line in Fig. 14(b) as well as in Fig. 14(a)] yields $\Omega_{t1} = 13.5$ that is in satisfactory agreement with the theoretical result. It is not clear why the Landau model does not seem to apply; but it may be too simplified since it does not anticipate a spatially and temporally chaotic convecting

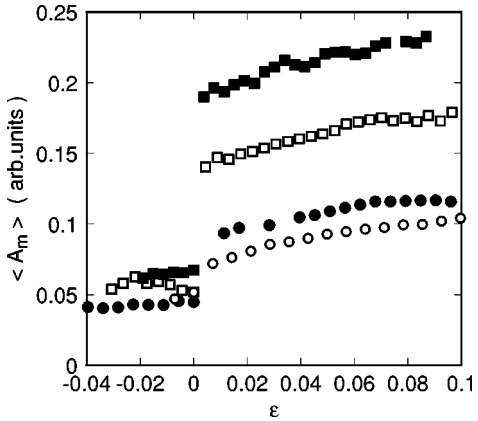

FIG. 13. The time average $\langle A_m \rangle(\Delta T)$ of $A_m(\Delta T,t)$ as a function of ϵ for $\Omega = 17.2$ (open circles), 29.5 (solid circles), 34.5 (open squares), and 44.2 (solid squares).

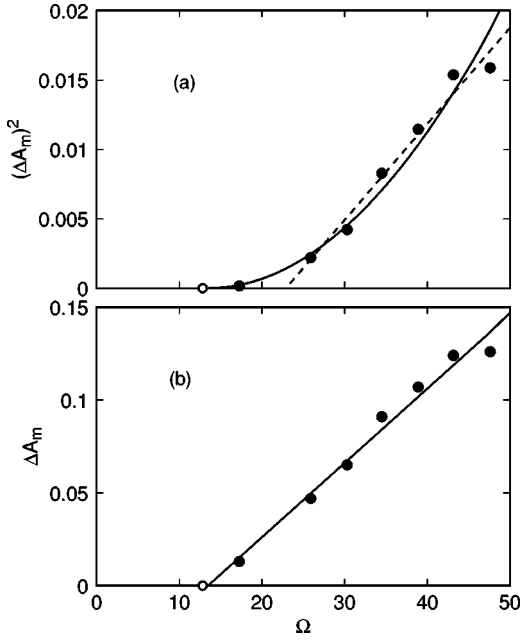

FIG. 14. The discontinuity ΔA_m, in arbitrary units, of $\langle A_m \rangle(\Delta T)$ at $\epsilon = 0$ as a function of Ω. The solid circles represent the experimental points. The open circle represents the theoretical value for the tricritical bifurcation. (a) gives $(\Delta A_m)^2$ vs Ω. The dashed line is a straight-line fit to the points for $\Omega \geqslant 25.9$. (b) shows ΔA_m vs Ω, and the straight solid line is a fit to all the data. This fit is also shown in (a) as a solid line.

state. As mentioned above, the region near the tricritical point should be the topic of additional experimental work in a cell more suitable for this parameter range.

The same procedure is followed for studying the finite-amplitude convection for $53 < \Omega < 150$. As is shown in Fig. 16, the bifurcation remains nonhysteretic. However, over this range the data do not show a clear jump in amplitude. Rather, $\langle A_m \rangle$ grows continuously, albeit very rapidly, as ΔT increases. Such a rapid increase of the amplitude would seem unlikely if the bifurcation were genuinely supercritical, and we assume that it remains subcritical as indicated by theory. Presumably the discontinuity in $\langle A_m \rangle$ is smoothed out by an inhomogeneity that arises above $\Omega \simeq 50$. A likely candidate for this inhomogeneity is the wall mode [19], which for large

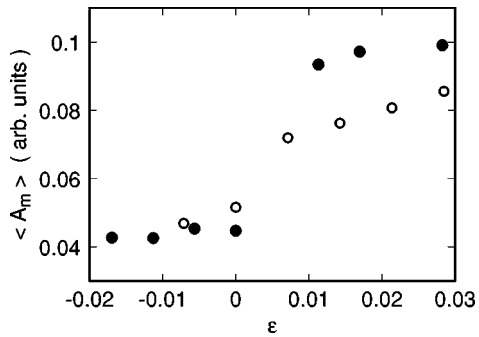

FIG. 15. The time average $\langle A_m \rangle(\Delta T)$ of $A_m(\Delta T,t)$ for $\Omega = 17.3$ (open circles) and 25.9 (solid circles) on an expanded horizontal scale.

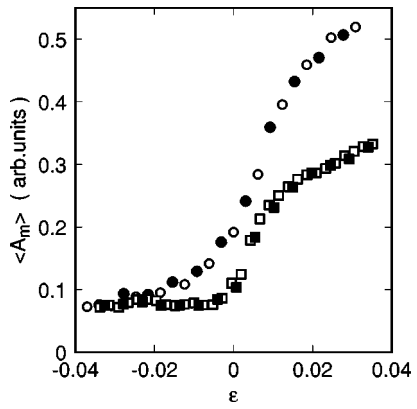

FIG. 16. The time average $\langle A_m \rangle(\Delta T)$ of $A_m(\Delta T,t)$ for $\Omega=68$ (squares) and $\Omega=120$ (circles). The open symbols represent increasing ΔT. The solid symbols represent decreasing ΔT.

Ω bifurcates from the conduction state before convection occurs in the bulk [22]. In the experiment, the bulk mode appeared first for Ω up to 53.2; but for our next-higher $\Omega=67.3$ the wall mode appeared before convection started in the system interior. The more gradual transition to the fully developed large-amplitude state introduces a somewhat larger uncertainty into the determination of the threshold; but this uncertainty still is only in the vicinity of 1%. The nature of the pattern just above onset was qualitatively similar to that of the patterns at lower Ω, as already shown in Fig. 7.

At $\Omega=53$ and close to onset, the dynamics of the patterns was different from what was observed at other Ω. Bursts of finite-amplitude convection appeared and then disappeared with a regular period of about $46\tau_\kappa$ but at different angular locations on a circle in the cell. A small part of the corresponding time series of A_m is shown in Fig 17(a). The power spectrum of the whole series of length $5290\tau_\kappa$ is shown in Fig 17(b). Strangely, we observed this periodic bursting only at $\Omega=53$.

For $\Omega \gtrsim 100$ it became more and more difficult to determine the bulk onset because, starting at $\Omega \simeq 60$, it was preceded by the appearance of the wall mode [19]. Here we describe the observed phenomena for Ω close to 400. Figure 18 shows an image of the entire cell for $\Omega=403$ and $r=28.96$. At this Ω, the expected Hopf bifurcation point is at $r_H=27.2$ and the stationary one at $r_s=34.1$. One sees that the wall mode penetrated far into the cell interior, leaving only a small central part for the observation of the bulk onset. In the counterclockwise-rotating frame of the apparatus, the wall mode traveled in the clockwise direction, with a frequency $\omega_w \simeq -19$. To a good approximation ω_w remained constant as r was increased from below the bulk onset to above. We define the wave number of the wall mode as $q_w=N/\Gamma$ where N is the number of wavelengths along the perimeter of the cell. For r close to the bulk onset q_w remained constant near 3.85. At higher r, the wall mode and the bulk pattern overlapped in the entire cell, and we could not measure ω_w and q_w beyond $r=30.25$.

When convection first appeared in the cell center, it had the form of small packets of traveling waves moving in random directions. Figure 19 shows images of the entire cell

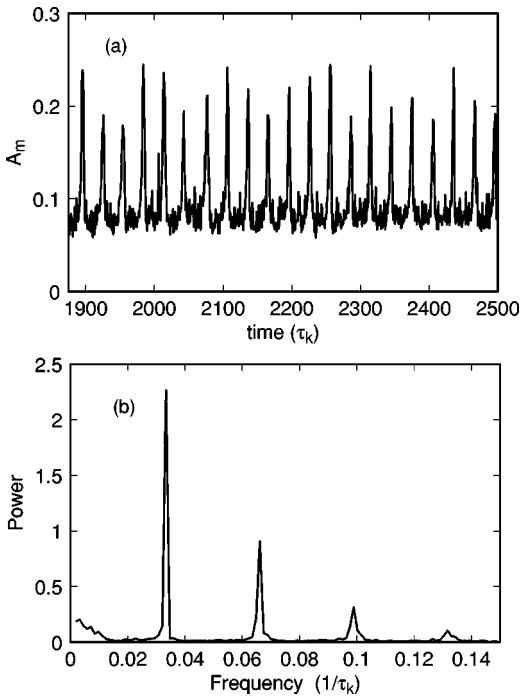

FIG. 17. (a) A part of the time series of A_m, in arbitrary units, observed at $\Omega=53$ and $\epsilon=0.004$. (b) The power spectrum of the entire time series at $\Omega=53$.

with $\Gamma=8.3$. By fitting a straight line to the variance of the $3.9d \times 3.9d$ square images in the center section, a slightly rounded onset at $r=29.43$ was found as shown in Fig. 20. As shown also in Fig. 21, the onset was well below r_s, but significantly above r_H. This is not surprising for a Hopf bifurcation in a finite system. When the bifurcation leads to traveling convection rolls, one has to distinguish between *convective* and *absolute* instability (see, e.g., [23]). For $r > r_H$ perturbations grow exponentially; but below the absolute instability at $r_a > r_H$ they travel away faster than they can grow and locally no structure evolves. In Fig. 20 r_a (see the Appendix) is shown as a vertical dash-dotted line. For a

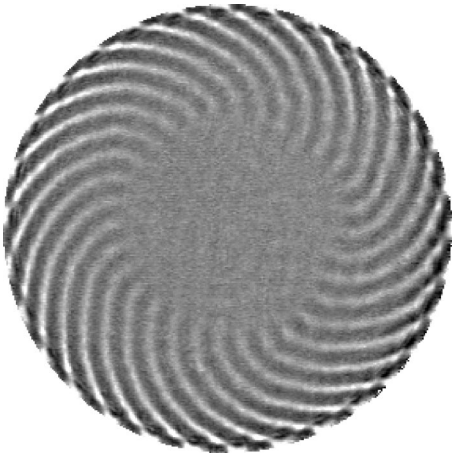

FIG. 18. A shadowgraph image of the entire cell for $\Omega=403$, $r=28.96$, and $\Gamma=8.3$.

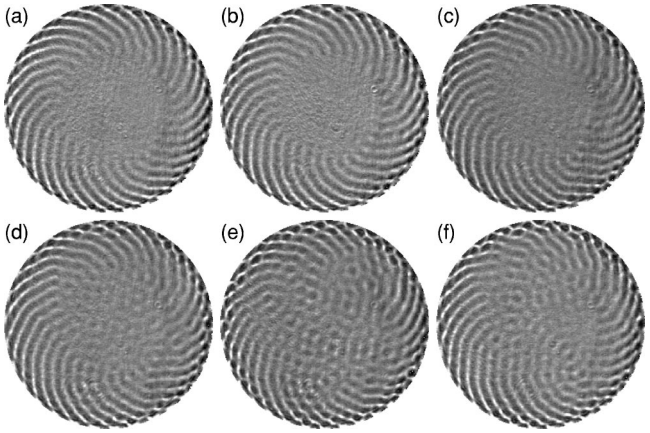

FIG. 19. Shadowgraph images of the cell with uniform spacing for $\Omega=403$, $\Gamma=8.3$, and $r=$ (a) 29.44, (b) 29.61, (c) 29.76, (d) 29.93, (e) 30.09, (f) 30.25.

finite system there will be an effective threshold r_{on}, with $r_H<r_{on}<r_a$, below which no convection rolls occur [24]. The value of r_{on} depends on the system size; above it the spatial extent of the system is sufficient to permit growth to macroscopic amplitude before the rolls leave the sample. For $r>r_a$ net growth occurs locally and convective structures generally will be observed.

In the $\Gamma=8.3$ cell, the interference from the wall mode prevented us from making a clean measurement of the traveling-wave frequency of the structure that appeared above r_{on}. Thus, to study the bulk onset in detail with less interference from the wall mode, we made another cell with larger aspect ratio $\Gamma=11.1$. It had a spacing of $d=3.96$ mm, which was only about 1% smaller than that of the $\Gamma=8.3$ cell. Images were obtained from $7.5d\times7.5d$ squares in the center. A typical time series of images at $\Omega=396$ just above onset at $r=29.8$ is shown in Fig. 22. The observed waves could be traveling or ''blinking'' or doing a combination of these. The frequency of the waves was found to be $\omega_b\simeq41$. Surprisingly, this is larger than the expected Hopf frequency $\omega=30.3$. As r increased, ω_b decreased and beyond $r=30.2$ only a time independent structure remained.

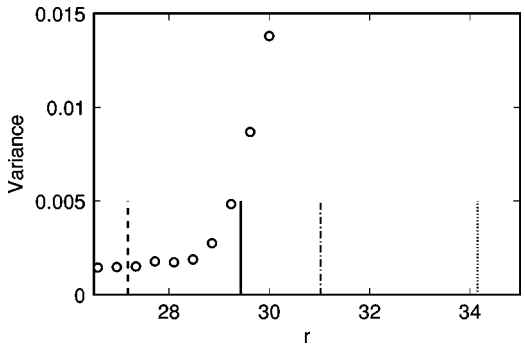

FIG. 20. Shadowgraph intensity for the central square of the cell with $\Gamma=8.3$ at $\Omega=403$. The vertical dashed, dash-dotted, and dotted lines are the theoretical convective (r_H), absolute (r_a), and stationary (r_s) bifurcation points, respectively. The solid line is the experimental onset.

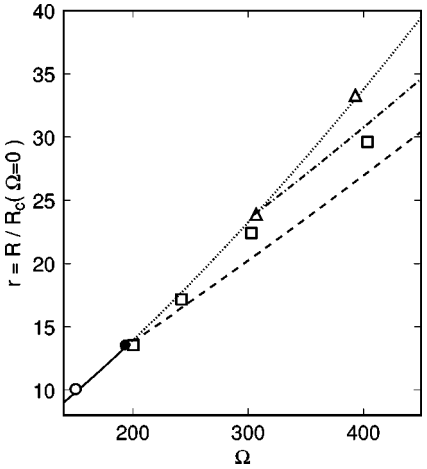

FIG. 21. A linear plot of the reduced critical Rayleigh number r_c at large Ω. The theoretical bifurcation lines are for $\sigma=0.185$, corresponding to the experiment in this Ω range. The dashed line is the primary Hopf bifurcation at r_H. The dash-dotted line is the absolute instability at r_a. The dotted line is the stability limit r_s to stationary perturbations of the conduction state in the Ω range where it is expected to be preceded by the primary Hopf bifurcation (dashed line). The open squares represent the onset of convection for $\Gamma=8.3$ in the presence of sidewalls and a traveling wall mode. The open triangles represent the onset of convection in the presence of a radial ramp of the cell spacing.

In an attempt to reduce the influence of the wall mode, we constructed two cells with a gentle radial ramp in the cell spacing for a radius $a>a_0$ with $a_0=28.6$ mm [25]. These cells had thicknesses in the uniform center section of $d_0=3.27$ mm and 3.93 mm, yielding $\Gamma_0=8.7$ and 7.3, respectively. Over the radius range $a_0<a<a_1=4.13$ cm the bottom plate had a quarter of a cosine profile of amplitude 0.66 mm. A paper sidewall was located radially 0.32 cm beyond a_1. Figure 23 shows the patterns that evolved in this case for $\Omega=307$ in the cell with $\Gamma=8.7$. Although the snapshots of

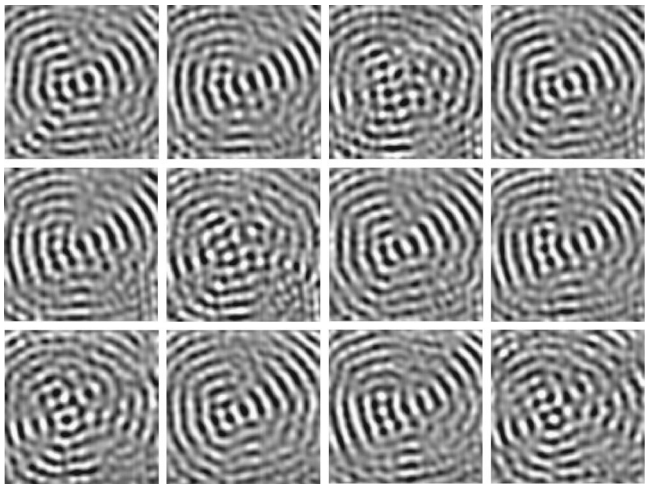

FIG. 22. Time series (from top left to right and then down) of images of the central $7.5d\times7.5d$ square for the $\Gamma=11.1$ cell at $r=29.8$ and $\Omega=396$. The time between images is 0.70 s, corresponding to $0.056\tau_\kappa$.

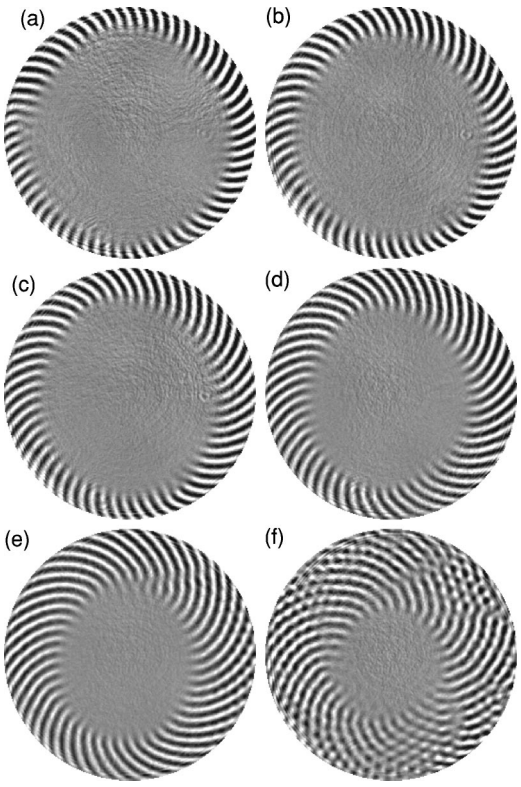

FIG. 23. Shadowgraph images of the cell with a gentle ramp in spacing for $\Omega=307$, $\Gamma=8.7$, and (a) $r=22.5$, (b) 22.6, (c) 22.7, (d) 23.1, (e) 23.4, (f) 23.43.

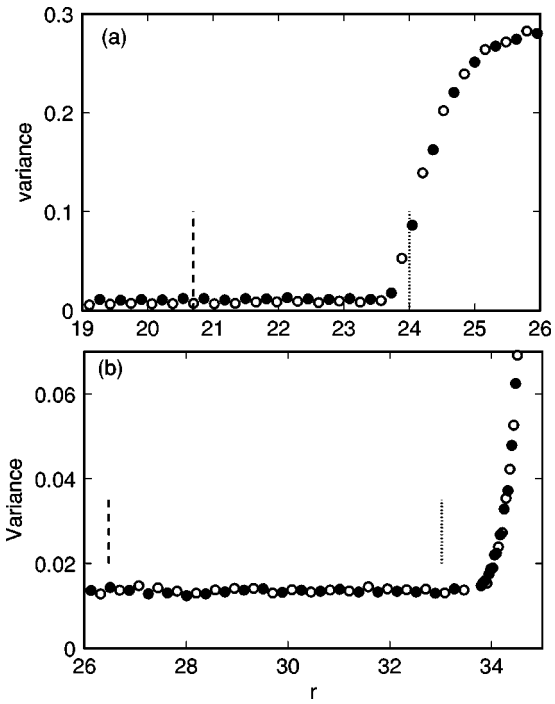

FIG. 24. The shadowgraph intensity for the cell with a gentle ramp in spacing for (a) $\Omega=307$, $\Gamma=8.7$ and (b) $\Omega=383$, $\Gamma=7.3$. Open (solid) circles are for increasing (decreasing) r. The dashed (dotted) vertical line indicates the expected location of the Hopf (stationary) bifurcation.

the system superficially look like those of the rigid-sidewall case Fig. 18, a striking difference is that the circumferential roll structure was *stationary* in the rotating frame of the cell [26]. The wave number of this structure was about twice that of the cell with uniform spacing. Thus this pattern is unrelated to the wall mode, and we presume that it is provoked by the inhomogeneity due to the centrifugal force and the radial ramp.

Square images of the central $5.6d\times5.6d$ of the cell were used to study the bulk onset. We found that the influence of the edge structure on the cell interior was much less than that of the wall mode. Figure 24 shows the bulk onsets for two values of Ω. Convection in the interior started at Rayleigh numbers that were larger than those for the uniform cells with rigid sidewalls. The experimental bulk bifurcation points are shown in Fig. 21 as open triangles. The onset was consistent with the stability limit at r_s of the conduction state to stationary perturbations, and well above r_H and r_a. Although the convective structures were time dependent, the spectrum of time series for the local intensity was broad band and we did not observe any characteristic frequencies. A typical time sequence of patterns is shown in Fig. 25. The patterns are reminiscent of those with fourfold coordination that had been observed at large Ω and $\sigma=O(1)$ in pure gases [9]. We have to conclude that the observations made in this cell are inconsistent with a Hopf bifurcation, and have no concrete explanation for this disagreement with the theoretical prediction for the laterally infinite uniform system.

V. SUMMARY

In this paper we reported on experimental and theoretical studies of convection at a Prandtl number $\sigma\approx0.18$ in the presence of rotation about a vertical axis. We reached this parameter value by using a 50% mixture of gaseous H_2 and Xe for the fluid [10]. In order to put the experimental results on a firm footing and to provide a direct comparison with theory, we carried out linear and weakly nonlinear bifurcation analyses of the Boussinesq equations [Eqs. (A3) in the Appendix] as a function of Ω. We also performed Galerkin analyses of Eqs. (A3) for the nonlinear straight-roll states

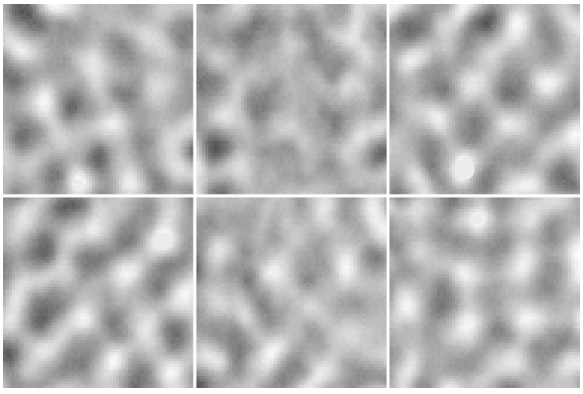

FIG. 25. Typical images above the bulk onset in a cell with a gentle ramp in spacing for $\Omega=383$, $\Gamma=7.3$, and $r=34.3$. On a time scale with arbitrary origin, the images were taken at $t=3.0$, 8.2, 9.5, 11.9, and 12.6 s.

corresponding to selected aspects of the problem.

For small Ω and in agreement with weakly nonlinear stability analysis, we found a supercritical bifurcation from the conduction state to the familiar Küppers-Lortz state of domain chaos. This parameter range deserves more detailed future experimental attention because our convection cells were not designed for its optimal study.

Above a tricritical rotation rate Ω_{t1} and in agreement with weakly nonlinear theory, the bifurcation was subcritical in the sense that it involved a discontinuous increase of the amplitude at onset ($\epsilon=0$); but the bifurcation was free of any detectable hysteresis. There were intermittent fluctuations between the ground state and the nonlinear convecting state when ΔT was kept within a fraction of a percent of the critical value, but no large-amplitude convection could be found below the onset when ΔT was decreased from above ΔT_c. The experimental patterns found above onset were time dependent and spatially disordered.

In contrast to the experimental observations, a Galerkin analysis yielded a saddlenode bifurcation to rolls at $\epsilon_{sa}<0$, which, over a wide range of Ω, was about 15% below the linear stability limit of the conduction state ($\epsilon=0$). Stability analysis of the nonlinear convecting state in the subcritical Ω range above and below $\epsilon=0$ showed that the patterns were Küppers-Lortz unstable. One might have expected finite-amplitude patterns above a Maxwell point which, for a quintic Landau equation for the straight-roll amplitude, is located at $\epsilon_T=0.75\epsilon_{sa}$. In the presence of rotation the system is nonpotential and the Maxwell point then corresponds to a value of ϵ where an interface between the ground state and the finite-amplitude state does not move.

Although it is not surprising that a disordered finite-amplitude state failed to evolve out of the ground state for $\epsilon<0$, one would have expected hysteresis in the sense that a finite-amplitude state prepared at $\epsilon>0$ would persist when lowering the control parameter to $\epsilon<0$. However, this problem was investigated recently for the one-dimensional quintic complex Ginzburg-Landau equation in the Benjamin-Feir unstable regime [27]. For that case the absence of hysteresis was demonstrated in some parameter regimes. Although this model is not directly related to rotating RBC, it shows explicitly that, in the case of a subcritical bifurcation where the finite amplitude state is unstable, hysteresis is not necessarily observable.

For $\Omega\gtrsim 50$ the formation of a bulk pattern was preceded by a wall mode [19] of traveling waves. Nonetheless, it was possible to study the bulk bifurcation in the system interior. For Ω values up to 120 or so there was still a very rapid rise of the amplitude at onset, but the transition was rounded and it was difficult to unambiguously assign a quantitative value to the amplitude discontinuity. We assume that the rounding is caused by the interaction of the bulk pattern with the wall mode.

For even higher rotation rates, with $\Omega>\Omega_{CD2}$, weakly nonlinar analysis predicts that the stationary bifurcation to convection should be preceded by a supercritical Hopf bifurcation. An experimental search for this phenomenon was somewhat indecisive. The problem is made more complicated because in a finite system a pattern will not form immediately above the convective instability; instead, ΔT must be increased to a value that depends on the system size but lies below the absolute instability [24]. We calculated the absolute instability line and found it to lie approximately 15% above the convective Hopf bifurcation point. In a cell with rigid sidewalls disordered time dependent convection was found, beginning about 10% above the convective instability, i.e., close to but below the absolute instability. However, the pattern was disordered and its frequency was a factor of 1.5 larger than the predicted Hopf-bifurcation frequency. This seems unusual since nonlinear dispersion usually (but not necessarily) reduces the frequency.

In an attempt to remove the wallmode influence on the system interior, we replaced the rigid sidewall of our cell with a gentle radial ramp of the cell spacing [25]. This was to suppress convection in and beyond the ramp. However, the ramp led to a well organized roll pattern localized radially near it. This pattern was stationary, and thus it was unrelated to the wall mode even though its spatial structure was similar. In the presence of the ramp, we found *no* evidence of convection in the cell center until the stationary instability point of the conduction state was reached. At that point, convection formed in the form of disordered cells with a tendency toward fourfold spatial coordination such as was found at larger σ. The observations made with this cell are inconsistent with the expected Hopf bifurcation. We do not know the reason for the difference between this system and the prediction for the laterally infinite uniform system, but can speculate that it may be associated with the large-scale flow induced by the radial ramp.

ACKNOWLEDGMENTS

We are grateful to F. Busse, P. Coullet, and L. Kramer for numerous stimulating discussions. This work was supported by U.S. Department of Energy Grant No. DE-FG03-87ER13738. Two of us (G.A. and W.P.) acknowledge support by NATO Linkage Grant No. CRG.LG.973103.

APPENDIX

In this section we present in more detail than in Sec. III the basic hydrodynamic equations and the calculational methods used in this paper. The theoretical description of thermal convection in binary fluids is well established [20]. The standard Boussinesq equations have to be generalized by including the concentration field C. Together with the temperature T it determines the density ρ according to

$$\rho(T,C)=\rho_0[1-\alpha(T-T_0)-\beta(C-C_0)], \qquad \text{(A1)}$$

with α and β the thermal and solutal expansion coefficients, respectively, and T_0, ρ_0, and C_0 the average values of temperature, density, and concentration, respectively. The diffusive part of the concentration current, $\mathbf{J}_c$, is driven by concentration gradients as well as by temperature gradients,

$$\mathbf{J}_c=D\left(\boldsymbol{\nabla} C+\frac{k_T}{T_0}\boldsymbol{\nabla} T\right), \qquad \text{(A2)}$$

with D the concentration diffusivity and k_T the thermal diffusion ratio that parametrizes the Soret effect, i.e., the generation of concentration currents by temperature variations. In principle, there exists a contribution of the concentration field to the heat current as well (the Dufour effect, see, e.g., Ref. [28]). However, consistent with previous investigations [10] the Dufour effect is negligible in our case and it does not modify noticeably any of the curves shown in this paper.

In nondimensionalized form [10,29] the Boussinesq equations (generalized by adding the Coriolis force proportional to the rotation frequency Ω) now read as follows:

$$\frac{1}{\sigma}D_t\mathbf{v}+2\Omega\mathbf{e}_z\times\mathbf{v}=-\boldsymbol{\nabla}\Pi+(\theta+c)\mathbf{e}_z+\Delta\mathbf{v},$$

$$D_t\theta=Rv_z+\Delta\theta, \tag{A3}$$

$$D_tc=R\Psi\mathbf{v}\cdot\mathbf{e}_z+\mathcal{L}(\Delta c-\Psi\Delta\theta),$$

with $\mathbf{v}$ the velocity and θ,Π,c the reduced deviations of temperature, pressure, concentration, respectively, from their conductive profiles. D_t denotes the total derivative $\partial_t+\mathbf{v}\cdot\boldsymbol{\nabla}$. The control parameters $R,\mathcal{L},\Psi$ have already been defined and interpreted in Sec. III. Equations (A3) have to be supplemented by the incompressibility condition $\boldsymbol{\nabla}\cdot\mathbf{v}=0$, which is automatically guaranteed by introducing the poloidal (f) and toroidal (g) velocity potentials as $\mathbf{u}=\boldsymbol{\nabla}\times\boldsymbol{\nabla}\times f\mathbf{e}_z+\boldsymbol{\nabla}\times g\mathbf{e}_z$. We use no-slip boundary conditions for $\mathbf{v}$ at the vertical boundaries $z=\pm d/2$. Instead of c the introduction of $\zeta=c-\Psi\theta$ is useful. It simplifies the notation of the nondimensionalized concentration current $\mathbf{J}_c=-\mathcal{L}\boldsymbol{\nabla}\zeta$ (A2), which like θ vanishes at the impermeable boundaries $z=\pm d/2$.

Let $\mathbf{V}(\mathbf{x},z,t)=(\theta,f,g,c)$ be a symbolic vector notation for the field variables in Eq. (A3). The onset of instability is obtained from a standard linear stability analysis of the basic state $\mathbf{V}=\mathbf{0}$. The ansatz $\mathbf{V}(x,z,t)=e^{\lambda t}e^{iqx}\mathbf{U}(q,z)$ diagonalizes the problem. The eigenvalue $\lambda(q,R)=\sigma(q,R)+i\omega(q,R)$ with the maximal real part σ determines the growth rate, which crosses zero at $R=R_c$ and $q=q_c$.

Let us first consider the case of large rotation frequency Ω, where we find a Hopf bifurcation [see Fig. (2)] with the critical Hopf frequency $\omega_c=\omega(R_c,q_c)$. To assess the resulting patterns in the weakly nonlinear regime we start as ususal from a superposition of left- and right-traveling waves,

$$\mathbf{V}(x,z,t)=[A(x,t)e^{i(q_cx+\omega_ct)}\mathbf{U}(q,z)+B(x,t)e^{i(q_cx-\omega_ct)}]\mathbf{U}^*(q,z)+\text{c.c.} \tag{A4}$$

The amplitude A of the left-traveling wave fulfills the equation

$$\tau_0(\partial_t-v_g\partial_x)A=\epsilon(1+ic_0)A+\xi_0^2(1+ic_1)\partial_{xx}A-(a_r+ia_i)|A|^2A-(b_r+ib_i)|B|^2A. \tag{A5}$$

The corresponding equation for the right-traveling amplitude B is obtained from Eq. (A5) by the substitutions: $v_g\rightarrow -v_g$, $A\leftrightarrow B$. All coefficients in Eq. (A5) have been calculated. They fulfill the condition $a_r+b_r>0$, $b_r<0$, which implies a supercritical bifurcation to stable standing waves as in the pure-fluid case [12]. According to the Newell criterion $a_r+c_1b_i>1$ applied to standing waves with $v_g=O(1)$ [30] the pattern is also Benjamin-Feir stable against long-wavelength modulation along the x axis.

As pointed out above (see Fig. 20), for a Hopf bifurcation one has to distinguish between *convective* and *absolute* instability (see, e.g., Ref. [23]). Within the GL approximation [23] the absolute instability is located at $\epsilon_a=r_a-1$ given by

$$\epsilon_a=\frac{\tau_0^2v_g^2}{4\xi_0^2(1+c_1^2)}. \tag{A6}$$

In the opposite case of small rotation frequencies Ω [see again Fig. (2)] the bifurcation is towards stationary rolls [$\omega(q_c,R_c)=0$]. Besides the amplitude B and the group velocity v_g the imaginary parts of all coefficients (i.e., c_0,c_1,a_i,b_i) vanish in Eq. (A5). When Ω is continuously increased from zero the coefficient a_r changes sign from positive to negative at a lower tricritical point Ω_{t1}, i.e., the bifurcation switches from supercritical to subcritical (see Fig. 1). The subcritical nonlinear periodic roll solutions have been calculated within an Galerkin approach for binary fluids, where we followed the unstable branch starting from the onset $\epsilon=0$ via the saddlenode towards the solutions at $\epsilon>0$. The Galerkin modes were chosen as in Ref. [29].

If one follows the stationary branch the coefficient a_r changes sign again at a second tricritcal point Ω_{t2} (see Fig. 1). There exists a codimension-two point at Ω_{CD2} where the critical Rayleigh numbers R_c of the stationary and oscillatory branch coincide (but the corresponding q_c remain different). In our case ($\sigma\simeq0.2$) the second tricritical point is irrelevant, since at the relevant Ω the Hopf bifurcation precedes the stationary bifurcation.

We have also performed a full nonlinear stability analysis of the periodic roll solutions within a Galerkin approach for the stationary branch. The rolls are always unstable against the short-wavelength Küppers-Lortz instability above $\Omega=\Omega_{KL}$. As a test we have alternatively identified the KL instability in the supercritical regime ($\Omega_{KL}<\Omega<\Omega_{t1}$) by calculating appropriate cross coefficients of coupled amplitude equations. In the subcritical regime $\Omega>\Omega_{t1}$ we observed in addition long-wavelength instabilities of the skewed-varicose type. The detailed analysis as well as the numerical simulations of Eqs. (A3) by using a pseudospectral code will appear in a separate paper. In general, all scenarios we found in the binary fluids match qualitatively the pure fluid case with rotation in the case of small σ.

[1] M.C. Cross and P.C. Hohenberg, Rev. Mod. Phys. **65**, 851 (1993).

[2] For a recent review of convection in gases, see E. Bodenschatz, W. Pesch, and G. Ahlers, Annu. Rev. Fluid Mech. **32**, 709 (2000).

[3] S. Chandrasekhar, *Hydrodynamics and Hydromagnetic Stability* (Oxford University Press, London, 1961).

[4] For a recent review of convection with rotation at small Prandtl numbers, see G. Ahlers and K. M. S. Bajaj, in *Proceedings of the IMA Workshop on Pattern Formation in Continuous and Coupled Systems*, edited by M. Golubitsky, D. Luss, and S. Strogatz (Springer, New York, 1999).

[5] G. Küppers and D. Lortz, J. Fluid Mech. **35**, 609 (1969); G. Küppers, Phys. Lett. **32A**, 7 (1970).

[6] R. Clever and F.H. Busse, J. Fluid Mech. **94**, 609 (1979).

[7] Y.-C. Hu, R.E. Ecke, and G. Ahlers, Phys. Rev. Lett. **74**, 5040 (1995).

[8] Y. Hu, W. Pesch, G. Ahlers, and R.E. Ecke, Phys. Rev. E **58**, 5821 (1998).

[9] K.M.S. Bajaj, J. Liu, B. Naberhuis, and G. Ahlers, Phys. Rev. Lett. **81**, 806 (1998).

[10] J. Liu and G. Ahlers, Phys. Rev. E **55**, 6950 (1997).

[11] G. Veronis, J. Fluid Mech. **24**, 545 (1966); **31**, 113 (1968).

[12] T. Clune and E. Knobloch, Phys. Rev. E **47**, 2536 (1993).

[13] R.M. Clever and F.H. Busse, Eur. J. Mech. B/Fluids **19**, 213 (2000).

[14] J.H.P. Dawes, Physica D **147**, 336 (2000); **149**, 197 (2001); J. Fluid Mech. **428**, 61 (2001).

[15] Calculations of the tricritical line by Clune and Knobloch (Ref. [12]) are inconsistent with the result of Ref. [6]. We recalculated the tricritical line and obtained the result shown in Fig. 1, which is more detailed than, but agrees with that of Ref. [6].

[16] J.R. deBruyn, E. Bodenschatz, S. Morris, S. Trainoff, Y.-C. Hu, D.S. Cannell, and G. Ahlers, Rev. Sci. Instrum. **67**, 2043 (1996).

[17] Diamond Turning Division, OFC Corporation, 69 Island Street, Keene, NH 03431 (603-357-7662).

[18] F.H. Busse, J. Fluid Mech. **30**, 625 (1967), for more recent values of the relevant coefficients, see Ref. [2], Sec. 6.5.

[19] F. Zhong, R.E. Ecke, and V. Steinberg, Phys. Rev. Lett. **67**, 2473 (1991); J. Fluid Mech. **249**, 135 (1993); R.E. Ecke, F. Zhong, and E. Knobloch, Europhys. Lett. **19**, 177 (1992); L. Ning and R.E. Ecke, Phys. Rev. E **47**, 3326 (1993); H.F. Goldstein, E. Knobloch, I. Mercader, and M. Net, J. Fluid Mech. **248**, 583 (1993); J. Herrmann and F.H. Busse, *ibid.* **255**, 183 (1993); E.Y. Kuo and M.C. Cross, Phys. Rev. E **47**, 2245 (1993); Y. Liu and R.E. Ecke, Phys. Rev. Lett. **78**, 4391 (1997).

[20] L.D. Landau and E.M. Lifshitz, *Fluid Mechanics* (Pergamon, London, 1959); J.K. Platten and J.C. Legros, *Convection in Liquids* (Springer, Berlin, 1984).

[21] Before selecting the maximum local amplitude A_m of an image, we convolved a 9x9 two-dimensional Gaussian window with the background-divided image to reduce digital noise.

[22] The wall mode does not contribute directly to the determination of A_m because it is localized near the wall and because A_m is selected from the pattern in the interior. To avoid a contribution at very large Ω where the wall mode extends further into the interior, we reduced the size of the square image used in the analysis so that its diagonal was only about 64% of the sample diameter.

[23] R.J. Deissler, J. Stat. Phys. **40**, 371 (1985); **54**, 1459 (1989); P. Huerre and P.A. Monkewitz, Annu. Rev. Fluid Mech. **22**, 473 (1990).

[24] See, for instance, Fig. 6 of K.L. Babcock, G. Ahlers, and D.S. Cannell, Phys. Rev. Lett. **67**, 3388 (1991); Phys. Rev. E **50**, 3670 (1994).

[25] K.M.S. Bajaj, N. Mukolobwiez, N. Currier, and G. Ahlers, Phys. Rev. Lett. **83**, 5282 (1999).

[26] The images in Fig. 23 of the wall mode in the cell with the ramp in the spacing are averages of 256 images taken over about 90 s. A similar averaging for the cell with the uniform spacing and the time dependent wall mode yielded an image without any structure.

[27] P. Coullet and L. Kramer (private communication).

[28] St. Hollinger and M. Lücke, Phys. Rev. E **52**, 642 (1995).

[29] B. Huke, M. Lücke, P. Büchel, and Ch. Jung, J. Fluid Mech. **408**, 121 (2000).

[30] H. Riecke and L. Kramer, Physica D **137**, 124 (2000).